

# Metal-to-Insulating Transition in the Perovskite System $\text{YSr}_2\text{Cu}_2\text{FeO}_{8-\delta}$ ( $0 < \delta < 1$ ) Modeled by DFT Methods

Marianela Gómez-Toledo, Sara A. López-Paz, Susana García-Martín, and M. Elena Arroyo-de Dompablo\*



Cite This: <https://doi.org/10.1021/acs.inorgchem.2c03475>



Read Online

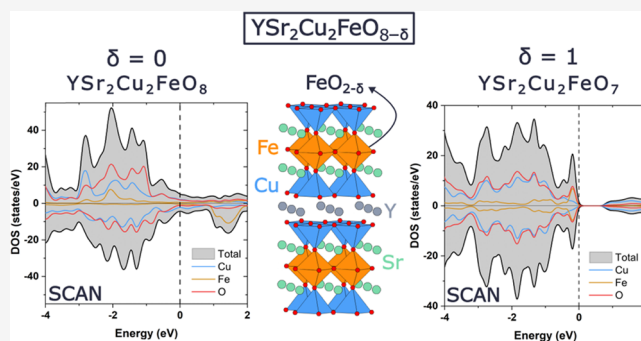
ACCESS |

Metrics & More

Article Recommendations

Supporting Information

**ABSTRACT:** Progress in the design of functional perovskite oxides relies on advances in density functional theory (DFT) methods to efficiently and effectively model complex systems composed of several transition-metal ions. This work reports the application of DFT methods to investigate the electronic structure of the  $\text{YSr}_2\text{Cu}_2\text{FeO}_{8-\delta}$  ( $0 < \delta < 1$ ) family in which the insulating, metal, or superconducting behaviors and even anion conductivity can be tuned by modifying the oxygen content. In particular, we assess the performance of the generalized gradient approximation (GGA), its Hubbard- $U$  correction (GGA +  $U$ ), and the strongly constrained and appropriately normed (SCAN) to model the metallic (idealized  $\text{YSr}_2\text{Cu}_2\text{FeO}_8$ ) and insulating (idealized  $\text{YSr}_2\text{Cu}_2\text{FeO}_7$ ) phases of the system. The analysis of the DFT results is supported by DC resistivity measurements that denote the metal character of the synthesized  $\text{YSr}_2\text{Cu}_2\text{FeO}_{7.86}$  and the semiconducting character of  $\text{YSr}_2\text{Cu}_2\text{FeO}_{7.08}$  prepared under reducing conditions. In addition, the band gap of  $\text{YSr}_2\text{Cu}_2\text{FeO}_{7.08}$ , in the range of 0.73–1.2 eV, has been extracted from diffuse reflectance spectroscopy (DRS). While the three methodologies (GGA, GGA +  $U$ , SCAN) permit the reproduction of the crystal structures of the synthesized oxides (determined here in the case of  $\text{YSr}_2\text{Cu}_2\text{FeO}_{7.08}$  by neutron powder diffraction (NPD)), the SCAN emerges as the only one capable to predict the basic electronic and magnetic properties across the  $\text{YSr}_2\text{Cu}_2\text{FeO}_{8-\delta}$  ( $0 < \delta < 1$ ) series. The picture that emerges for the metal ( $\delta = 0$ ) to insulating ( $\delta = 1$ ) transition is the one in which oxygen vacancies contribute electrons to the filling of the Cu/Fe- $3d_{x^2-y^2}$  states of the conduction band. These results validate the SCAN functional for future DFT investigations of complex functional oxides that combine several transition metals.



## 1. INTRODUCTION

Perovskite-type oxides ( $\text{ABO}_3$  and related materials) exhibit a broad range of functional properties that derive in multiple and relevant applications.<sup>1</sup> To better understand the properties and optimize the applications of these oxides, a profound knowledge of their crystal and electronic-structure relationships is compulsory. Nowadays, electronic-structure calculations based on density functional theory (DFT) are extensively applied to successfully predict and design materials with particular properties. Since the development of DFT by Hohenberg, Kohn, and Sham,<sup>2,3</sup> a great deal of improvement on exchange-correlation (XC) functionals has been reported, such as the widely used generalized gradient approximation (GGA) developed in the late 1980s.<sup>4,5</sup> The GGA functionals have offered some acceptable results in the modeling of perovskite oxides based on  $d^0$  transition metals (TM).<sup>6–9</sup> However, the overestimation of electron delocalization and metallic character is a known failure of DFT methods for systems with localized and strongly interacting  $d$ -electrons and  $f$ -electrons.<sup>10–13</sup> In the 1990s, the DFT +  $U$  method

introduced an explicit treatment of electron correlation with a Hubbard-like model for a subset of states in the system.<sup>10,14</sup> Vast literature demonstrates the suitability of the DFT +  $U$  approach to investigate TM oxides with strong Coulomb correlations. More recently, the strongly constrained and appropriately normed (SCAN) meta-GGA functional<sup>15</sup> has shown good performance to model the basic physical properties and phenomena associated to correlated oxides.<sup>16,17</sup> For instance, investigations on perovskite-related oxides using meta-GGA functionals (and particularly SCAN) have accurately described the transition from the insulating to the metallic character of  $\text{La}_2\text{CuO}_4$  by substitution of La by Sr in the superconducting system;<sup>18</sup> the layered ordering stabiliza-

Received: September 30, 2022

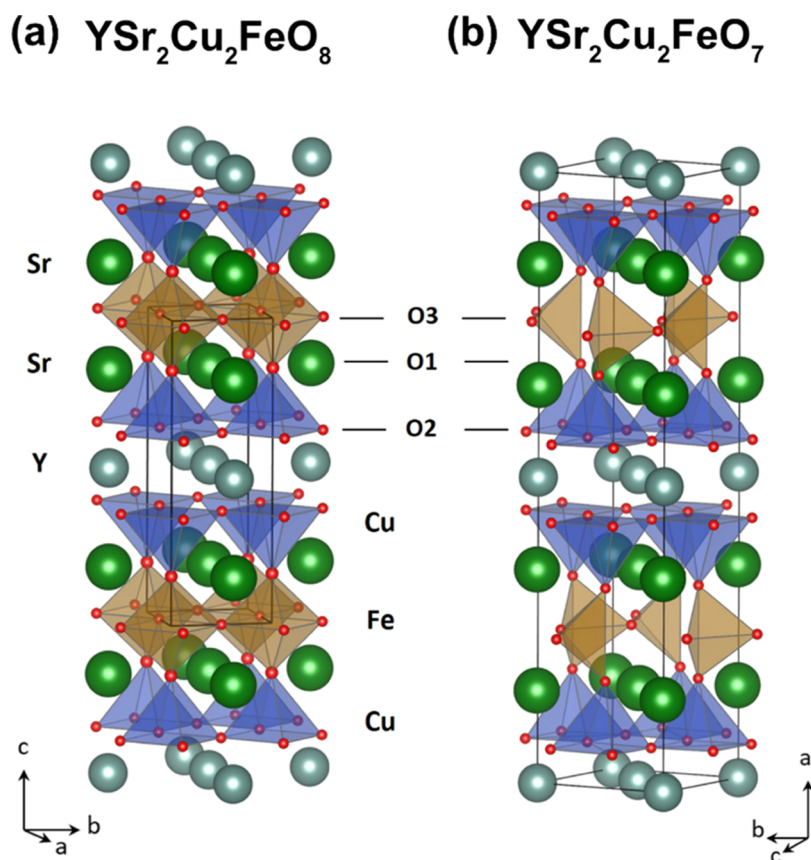


**Figure 1.** Crystal structure representations of (a) idealized stoichiometric oxide  $\text{YSr}_2\text{Cu}_2\text{FeO}_8$  ( $a_p \times a_p \times 3a_p$  unit cell, S.G.  $P4/mmm$ ) and (b) idealized stoichiometric oxide  $\text{YSr}_2\text{Cu}_2\text{FeO}_7$  ( $6a_p \times \sqrt{2}a_p \times \sqrt{2}a_p$  unit cell, S.G.  $Ima2$ ).

tion of the  $\text{Bi}_2\text{MFeO}_6$  perovskites ( $M = \text{Al, Ga, In}$ ) induced by the Fe–magnetic interactions;<sup>19</sup> the effect of the hole and electron doping in the electronic structure of  $\text{Sm}_{1-x}\text{M}_x\text{NiO}_3$  ( $M = \text{Ca, Ce}$ );<sup>20</sup> and have predicted the structural cubic-symmetry breaking, band-gap existence, and magnetic behavior in  $\text{ABO}_3$  perovskites with  $B = 3d\text{-TM}$ .<sup>21</sup>

Despite the substantial progress in the computational investigation of perovskites, the scenario complicates when different TM ions occupy the B positions, even if this occurs in an ordered manner. Hence, assessing the performance of DFT methodologies and, specifically, of the recently developed SCAN functional at a basic property-level prediction—crystal, electronic, and magnetic structures—is a prerequisite to further investigating the particular properties of complex perovskite oxides. In the present work, we focus on the  $\text{YSr}_2\text{Cu}_2\text{FeO}_{8-\delta}$  ( $0 < \delta < 1$ ) family derived from the so-called “YBaCuO” superconducting cuprates.<sup>22,23</sup> Figure 1a,b displays the graphic representation of the crystal structure of the idealized stoichiometric endmembers  $\text{YSr}_2\text{Cu}_2\text{FeO}_8$  and  $\text{YSr}_2\text{Cu}_2\text{FeO}_7$  ( $\delta = 0$  and  $1$ , respectively). The structures consist of an alternation of  $\text{FeO}_{2-\delta}/\text{SrO}/\text{CuO}_2/\text{Y}/\text{CuO}_2/\text{SrO}$  layers along the  $c$ -axis or  $a$ -axis (space group (S.G.)  $P4/mmm$  and S.G.  $Ima2$  settings, respectively). The idealized  $\text{YSr}_2\text{Cu}_2\text{FeO}_8$ , with  $[\text{FeO}_6]$  octahedral units in the Fe layers, presents a tetragonal (S.G.  $P4/mmm$ ) crystal structure with  $a_p \times a_p \times 3a_p$  unit cell dimensions ( $a_p$  refers to the lattice parameter of the cubic perovskite structure).<sup>24</sup> Lowering the oxygen content ( $\delta > 0$ ) creates vacancies in the O3 positions of the  $\text{FeO}_{2-\delta}$  layer (Figure 1) so that in the  $\text{YSr}_2\text{Cu}_2\text{FeO}_{8-\delta}$  family, the Fe atoms may adopt octahedral, tetrahedral, and/or

square pyramid coordination.<sup>23–27</sup> In combination with the Y and Sr ordering, there is layered ordering of the coordination polyhedra (octahedra O, square pyramid SP, and tetrahedra T) around the Fe and Cu atoms in the manner O/SP/SP/O in the idealized  $\text{YSr}_2\text{Cu}_2\text{FeO}_8$  and like T/SP/SP/T in the idealized  $\text{YSr}_2\text{Cu}_2\text{FeO}_7$ . In addition, in the idealized  $\text{YSr}_2\text{Cu}_2\text{FeO}_7$ , the different orientation of the tetrahedral coordination polyhedra of the Fe atoms leads to a sixfold superstructure ( $6a_p \times \sqrt{2}a_p \times \sqrt{2}a_p$  within the  $Ima2$  space group).<sup>23,28</sup>

$\text{YSr}_2\text{Cu}_2\text{FeO}_{8-\delta}$  ( $0 < \delta < 1$ ) compounds show a non-stoichiometric anion sublattice resulting from the interplay between different oxidation states of Fe and Cu atoms.<sup>22,23,29</sup> Oxides of the system, with different oxygen content and properties, have already been reported. The highly oxidized term  $\text{YSr}_2\text{Cu}_2\text{FeO}_{7.85}$  obtained experimentally in ozone flow, with Fe in the unusual 4+ formal oxidation state and mixed  $\text{Cu}^{3+}$  and  $\text{Cu}^{2+}$  valences, is a metallic oxide with a superconducting transition at  $T_c = 70$  K.<sup>24</sup> The compound presents magnetic ordering arising from the ferromagnetic (FR) interactions below  $T_N = 110$  K between  $\text{Fe}^{4+}$  cations with parallel in-plane spins in the  $\text{FeO}_{2-\delta}$  layers coupled with a soft character of the antiferromagnetic (AFM) interactions between layers.<sup>24</sup> The low oxygen content terms  $\text{YSr}_2\text{Cu}_2\text{FeO}_{7.08}$ ,<sup>27</sup>  $\text{YSr}_2\text{Cu}_2\text{FeO}_{7.11}$ ,<sup>28</sup> and  $\text{YSr}_2\text{Cu}_2\text{FeO}_{7.04}$ ,<sup>26</sup> prepared under reducing conditions, are insulators with mainly  $\text{Fe}^{3+}$  and  $\text{Cu}^{2+}$ . In between those extremes, air-synthesized  $\text{YSr}_2\text{Cu}_2\text{FeO}_{7.56}$  mixed valence  $\text{Fe}^{3+}/\text{Fe}^{4+}$  and  $\text{Cu}^{2+}/\text{Cu}^{3+}$  oxide, exhibits an interesting electrochemical behavior associated with catalytic activity in the oxygen reduction

reaction (ORR), being a potential air electrode for solid oxide fuel cells (SOFCs).<sup>26,27</sup>

Modeling the evolution of the electronic structure of  $\text{YSr}_2\text{Cu}_2\text{FeO}_{8-\delta}$  from the metallic phase ( $\delta \sim 0$ ) to the insulating one ( $\delta \sim 1$ ), which is to say, the metal-to-insulating transition as a function of the oxygen content, constitutes a challenge for DFT methods, apart from the relevance of tuning the electronic properties of these materials to manage particular applications. Indeed, few computational works deal with the two facts that are found in  $\text{YSr}_2\text{Cu}_2\text{FeO}_{8-\delta}$  oxides: first, the combination of two transition-metal ions in the B positions of the crystal structure, and second, the occurrence of oxygen nonstoichiometry. Both aspects highly condition the electronic properties of the materials.

We here report DFT calculations for the idealized stoichiometric compounds  $\text{YSr}_2\text{Cu}_2\text{FeO}_8$  and  $\text{YSr}_2\text{Cu}_2\text{FeO}_7$  as representatives of the experimentally obtained  $\text{YSr}_2\text{Cu}_2\text{FeO}_{7.85}$  and  $\text{YSr}_2\text{Cu}_2\text{FeO}_{7.08}$ . The calculations have been performed within the GGA-Perdew, Burke, and Ernzerhof (PBE) functional (hereafter denoted as simply GGA), its Hubbard correction PBE +  $U$  (denoted as GGA +  $U$ ), and the meta-GGA-SCAN functional (denoted as SCAN). We demonstrate that the three methodologies fairly reproduce the crystal structures. However, the prediction of the electrical and magnetic properties depends on the functional used for the calculation. While the metallic behavior and magnetic features of the  $\text{YSr}_2\text{Cu}_2\text{FeO}_8$  phase are well described with the GGA and SCAN functionals, the SCAN and GGA +  $U$  offer the best approaches to investigate the  $\text{YSr}_2\text{Cu}_2\text{FeO}_7$  compound. We also support the electronic-structure calculations with resistivity experiments that confirm the metal-to-insulating transition in the  $\text{YSr}_2\text{Cu}_2\text{FeO}_{8-\delta}$  ( $0 < \delta < 1$ ) system. In addition, the optical band gap of  $\text{YSr}_2\text{Cu}_2\text{FeO}_{7.08}$  has been determined from diffuse reflectance spectroscopy (DRS).

## 2. METHODOLOGY

**2.1. Experimental Section.** Our previous works cover the synthesis and structural characterization of several  $\text{YSr}_2\text{Cu}_2\text{FeO}_{8-\delta}$  oxides.<sup>24,27,30</sup> In this work, polycrystalline  $\text{YSr}_2\text{Cu}_2\text{FeO}_{8-\delta}$  ( $\delta = 0.15$  and  $0.92$ ) compounds have been prepared by the conventional ceramic method in air. The intimate mixtures of  $\text{Fe}_2\text{O}_3$  (Aldrich 99.99%),  $\text{CuO}$  (Aldrich 99.9999%), previously decarbonated  $\text{Y}_2\text{O}_3$  (Aldrich 99.9%), and previously dehydrated  $\text{SrCO}_3$  (Aldrich 99.9%) in the stoichiometric relations were subjected to an initial treatment at 1173 K for 12 h in air. The resulting powders were ground in an agate mortar, pelletized, and subjected to several treatments at 1253 K in air, for 72 h, with intermediate grindings. The air-prepared sample was heated at 1023 K for 24 h in  $\text{N}_2$  flow to obtain  $\text{YSr}_2\text{Cu}_2\text{FeO}_{7.08}$  oxide and the  $\text{N}_2$  prepared compound was oxidized in ozone at 473 K to obtain  $\text{YSr}_2\text{Cu}_2\text{FeO}_{7.85}$ .

The crystal structure of the  $\text{YSr}_2\text{Cu}_2\text{FeO}_{7.08}$  compound at room temperature (RT) was determined by neutron powder diffraction (NPD) using the high-resolution D2B instrument at the ILL (Grenoble, France) with a wavelength of  $\lambda = 1.594$  Å. Rietveld refinements were performed following the Fullprof software.<sup>31</sup>

DC electrical resistivity measurements of sintered pellets of  $\text{YSr}_2\text{Cu}_2\text{FeO}_{7.85}$  and  $\text{YSr}_2\text{Cu}_2\text{FeO}_{7.08}$  have been performed in the temperature region  $5 < T < 300$  K using a Quantum Design PPMS device. Four-probe electrical contacts were made using conductive mixed silver paste and gold wires. The

resistivity was measured in sweep mode with a heating rate of 2 K/min.

DRS measurements have been carried out to determine the optical band gap in  $\text{YSr}_2\text{Cu}_2\text{FeO}_{7.08}$ . The experiments have been performed in a Cary 5G spectrophotometer with an external integrating sphere. The measurement range was 300–3300 nm and the data interval was 1 nm. As stated by Kubelka and Munk,<sup>32</sup> diffuse reflectance spectra can be transformed into absorption spectra through the Kubelka–Munk function ( $F(R_\infty)$ , eq 1)

$$F(R_\infty) = \frac{K}{S} = \frac{(1 - R_\infty)^2}{2R_\infty} \quad (1)$$

where  $R_\infty$  is the absolute reflectance of an infinitely thick specimen and  $K$  and  $S$  are the absorption and scattering coefficients, respectively.  $F(R_\infty)$  is proportional to the extinction coefficient ( $\alpha$ ), which can be expressed by eq 2, according to the Tauc method<sup>33</sup>

$$(\alpha h\nu)^{1/\gamma} = A(h\nu - E_g) \quad (2)$$

where  $h$  is the Planck constant,  $\nu$  is the photon frequency,  $E_g$  is the band-gap energy, and  $A$  is a constant. The  $\gamma$  factor considers the nature of the electronic transition, being equal to 1/2 for allowed direct and 2 for allowed indirect transition.

Replacing  $\alpha$  with  $F(R_\infty)$  results in the following expression (eq 3)

$$F(R_\infty)(h\nu)^{1/\gamma} = A(h\nu - E_g) \quad (3)$$

The band gap can thus be extracted from diffuse reflectance spectra transformed according to eq 3. Linear fitting of the Tauc plot followed by extrapolating to the  $x$ -axis intersection gives the band-gap value.

**2.2. Computational Section.** Calculations for the idealized stoichiometric endmembers of the  $\text{YSr}_2\text{Cu}_2\text{FeO}_{8-\delta}$  family,  $\text{YSr}_2\text{Cu}_2\text{FeO}_8$  and  $\text{YSr}_2\text{Cu}_2\text{FeO}_7$ , have been performed using the *ab initio* total-energy and molecular dynamics program Vienna *ab initio* simulation package (VASP) developed at the Universität Wien.<sup>34,35</sup> The interaction of core electrons with the nuclei is described by the projector augmented wave (PAW) method<sup>36</sup> with  $2s^2 2p^4$  of O,  $3s^2 3p^6 3d^7 4s^1$  of Fe,  $3p^6 3d^{10} 4p^1$  of Cu,  $4s^2 4p^6 5s^2$  of Sr, and  $4s^2 4p^6 4d^1 5s^2$  of Y treated as valence electrons. For the GGA approximation, we selected the exchange and correlation functional form developed by Perdew, Burke, and Ernzerhof (PBE).<sup>37</sup> On the other hand, for the meta-GGA approximation, the strongly constrained and appropriately normed (SCAN)<sup>15</sup> functional was used. In all cases, the energy cut off for the plane wave basis set was kept fixed at a constant value of 600 eV throughout the calculations. The integration in the Brillouin zone is done on appropriate sets of  $k$ -points determined by the Monkhorst–Pack scheme. The  $k$ -point meshes were set at  $2 \times 8 \times 8$  for  $\text{YSr}_2\text{Cu}_2\text{FeO}_7$  and  $10 \times 10 \times 4$  for  $\text{YSr}_2\text{Cu}_2\text{FeO}_8$ , using a Gaussian smearing parameter of 0.05 eV. For the density of states (DOS) calculations, the tetrahedron method with Blöchl corrections<sup>38</sup> was used. Self-consistency was achieved with a tolerance in total energy of  $1 \times 10^{-4}$  eV for geometry optimization and  $1 \times 10^{-6}$  eV for DOS calculations.

A local Hubbard- $U$  (GGA +  $U$ ) was added to Fe and Cu atoms following the simplified rotationally invariant framework developed by Dudarev et al.<sup>39</sup> Typically,  $U$  is formulated as  $U_{\text{eff}}$

**Table 1.** Atomic Positions and Cell Parameters Obtained from the Rietveld Refinement of the NPD Data for  $\text{YSr}_2\text{Cu}_2\text{FeO}_{7.08}$ <sup>a</sup>

atom	site	<i>x</i>	<i>y</i>	<i>z</i>	Biso (Å)	occ.
Y	4a	0	0	0	0.20(4)	1
Sr	8h	0	0.34911(7)	0.0067(8)	0.68(4)	1
Fe1/Cu1	8i	0.0440(8)	0.25	0.5584(5)	1.0(7)	0.426(7)/0.074(7)
Cu2/Fe2	8h	0	0.42610(8)	0.5000(5)	0.28(3)	0.85(1)/0.15(1)
O1	8h	0	0.3257(1)	0.4739(7)	1.30(5)	1
O2a	8g	0.25	0.0630(1)	0.25	0.39(2)	1
O2b	8g	0.25	−0.0649(1)	0.25	0.39(2)	1
O3	8i	0.390(1)	0.25	0.616(1)	2.1(1)	0.574(3)

<sup>a</sup>S.G. *Imma* (no. 74); *a* = 5.4053(1) Å, *b* = 22.9136(5) Å, *c* = 5.4577(1) Å, *V* = 675.98(2) Å<sup>3</sup>,  $\delta$  = 0.92; *R*<sub>p</sub> = 3.62%; *R*<sub>wp</sub> = 4.66%;  $\chi^2$  = 4.22.

= *U* − *J*, where *U* is the onsite Coulomb term and *J* the exchange term. In this work, this effective parameter is simply referred to as *U*. The *J* value was fixed to 1 eV. An effective *U* value of 4 eV was used for the *d* orbitals of Cu and Fe, that were found appropriate in previous GGA + *U* investigations.<sup>13,40–42</sup> The local magnetic moments are taken from the difference between the projected electron density of up and down spins onto 1 Å radius sphere. Bader charge analysis<sup>43</sup> was performed on the charge density files<sup>44</sup> using the pymatgen package.<sup>45</sup>

In the present work, we have performed calculations using the idealized stoichiometric compositions  $\text{YSr}_2\text{Cu}_2\text{FeO}_7$  and  $\text{YSr}_2\text{Cu}_2\text{FeO}_8$  and perfect Cu/Fe ordering within the crystal structures. The crystallographic model of  $\text{YSr}_2\text{Cu}_2\text{FeO}_8$  oxide has been constructed taking the initial positions from  $\text{YSr}_2\text{Cu}_2\text{FeO}_{7.86}$  (ICSD file 11514),<sup>24</sup> considering a ferromagnetic  $2 \times 2 \times 1$  superstructure of the tetragonal  $a_p \times a_p \times 3a_p$  unit cell shown in Figure 1a (that is,  $\text{Y}_4\text{Sr}_8\text{Cu}_8\text{Fe}_4\text{O}_{32}$  composition). For  $\text{YSr}_2\text{Cu}_2\text{FeO}_7$  oxide, the  $6a_p \times \sqrt{2}a_p \times \sqrt{2}a_p$  (S.G. *Ima2*) unit cell has been used for the calculations ( $\text{Y}_4\text{Sr}_8\text{Cu}_8\text{Fe}_4\text{O}_{28}$ ), corresponding to an ideal arrangement of the tetrahedral chains (Figure 1b). The initial cell parameters and atomic positions of  $\text{YSr}_2\text{Cu}_2\text{FeO}_7$  were taken from the ICSD record of isostructural  $\text{YSr}_2\text{Cu}_2\text{GaO}_7$ .<sup>46</sup> Although the magnetic structure of  $\text{YSr}_2\text{Cu}_2\text{FeO}_{8-\delta}$  phases with high  $\delta$  values ( $\delta \sim 1$ ) has not yet been experimentally determined, magnetic interactions associated to  $\text{Fe}^{3+}$  and  $\text{Cu}^{2+}$  cations are expected, and, as explained below, different magnetic structures have been considered.

### 3. RESULTS AND DISCUSSION

**3.1. Experimental Section.** The crystal structure and superconducting behavior of the compound with the highest oxygen content,  $\text{YSr}_2\text{Cu}_2\text{FeO}_{7.86}$ , has previously been reported.<sup>24</sup> In this work, the crystal structure of  $\text{YSr}_2\text{Cu}_2\text{FeO}_{7.08}$  is refined by NPD. Table 1 lists the results of the Rietveld refinement of the NPD pattern of  $\text{YSr}_2\text{Cu}_2\text{FeO}_{7.08}$  (Figure 2). The refined occupation factors of 8i and 8h crystallographic positions reveal certain disorder (antisite location) of the Fe and Cu atoms. Note that consistently with the oxygen content ( $\delta = 0.92$  in  $\text{YSr}_2\text{Cu}_2\text{FeO}_{8-\delta}$ ), there is an occupation of 0.574 for O3 in 8i positions. In the idealized term  $\delta = 1$  ( $\text{YSr}_2\text{Cu}_2\text{FeO}_7$ ) where only tetrahedral-Fe is present, the fractional occupancy of O3 is of 0.5. Importantly, the results indicate that corrugation of the  $[\text{FeO}_4]$  tetrahedral units and their relative orientation along the stacking direction originate an additional superstructure with a diagonal orthorhombic unit cell of dimensions  $\sqrt{2}a_p \times 6a_p \times \sqrt{2}a_p$  in the *Imma* space group (note the change of S.G. setting as described in Table 2). Therefore, the refined crystal structure of  $\text{YSr}_2\text{Cu}_2\text{FeO}_{7.08}$  is

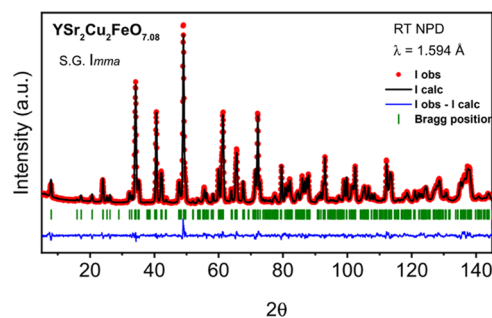


**Figure 2.** Rietveld refinement of the room temperature (RT) NPD pattern of  $\text{YSr}_2\text{Cu}_2\text{FeO}_{7.08}$ .

in close agreement with the one reported by Mochiku et al. (ICSD file 151653) for the  $\text{YSr}_2\text{Cu}_2\text{FeO}_{7.11}$  compound.<sup>28</sup> The crystallographic model with the *Imma* space group accounts for the presence of two types of tetrahedral chains in the Fe layers, which are left- and right-hand rotated. In this sense, the crystal structure of  $\text{YSr}_2\text{Cu}_2\text{FeO}_{7.08}$  can be considered as a disordered version of the model crystal structure of the stoichiometric  $\text{YSr}_2\text{Cu}_2\text{GaO}_7$  determined by Roth et al. (ICSD file 71263, used for the DFT calculations)<sup>46</sup> in which the presence of a single chain orientation is well captured within the *Ima2* space group, as it is represented in Figure 1b.

The variation of the resistivity with the temperature of  $\text{YSr}_2\text{Cu}_2\text{FeO}_{7.86}$  shows the expected superconducting/metallic transition at  $T_c = 70$  K (Figure 3a).<sup>24</sup> Above the  $T_c$ , the increase of the electrical resistance with temperature reflects the metallic character (inset in Figure 3a). On the contrary,  $\text{YSr}_2\text{Cu}_2\text{FeO}_{7.08}$  oxide presents a semiconducting/insulating transition near 200 K (Figure 3b). The logarithmic plot of resistance (inset in Figure 3b) shows an activated behavior in the 200–300 K temperature range, with an activation energy ( $E_a$ ) of 0.147(4) eV.

The optical band gap of the  $\text{YSr}_2\text{Cu}_2\text{FeO}_{7.08}$  phase has been extracted from DRS measurements. The Tauc plot and Kubelka–Munk analysis offer an approximate estimation of optical band gap.<sup>32,33,47</sup> However, if the nature of the electronic transition is not well known (as in the present case), the  $\gamma$  parameter (eq 2) value becomes an important source of uncertainty. For  $\text{YSr}_2\text{Cu}_2\text{FeO}_{7.08}$ , considering a direct allowed electronic transition, from the Tauc plot we derive a band-gap value of 1.2 eV, while a band gap of 0.73 eV results if an indirect electronic transition is considered (Figure 3c). Methods such as photoluminescence (PL)<sup>48</sup> and X-ray photoelectron spectroscopy (XPS)<sup>49</sup> that offer an accurate band-gap determination are out of the scope of this paper. Given the above, this work considers the interval 1.2–0.73 eV

**Table 2. Calculated Unit Cell Parameters (Å), Unit Cell Volume (Å<sup>3</sup>), Volume per Atom (Å<sup>3</sup>), and Selected Bond Lengths (Å) for YSr<sub>2</sub>Cu<sub>2</sub>FeO<sub>7</sub> and YSr<sub>2</sub>Cu<sub>2</sub>FeO<sub>8</sub> Idealized Oxides<sup>a</sup>**

	experimental YSr <sub>2</sub> FeCu <sub>2</sub> O <sub>7.85</sub>	GGA	GGA + U	SCAN	YSr <sub>2</sub> FeCu <sub>2</sub> O <sub>7</sub>	experimental <sup>b</sup> YSr <sub>2</sub> FeCu <sub>2</sub> O <sub>7.08</sub>	C-AF GGA	C-AF GGA + U	C-AF SCAN
<i>a</i> , <i>b</i>	3.8145(3)	3.8252	3.8315	3.7861	<i>a</i>	22.9136(5) <sup>b</sup>	23.1337	23.1424	22.8529
<i>c</i>	11.327(7)	11.3803	11.5457	11.2755	<i>b</i>	5.4577(1) <sup>b</sup>	5.5007	5.5069	5.4411
<i>V</i>	164.81(1)	166.52	169.50	161.62	<i>c</i>	5.4053(1) <sup>b</sup>	5.4241	5.4265	5.3744
<i>V</i> per atom	11.77	11.89	12.10	11.54	<i>V</i>	675.98(2)	690.13	691.63	668.22
<i>d</i> Fe–O3	1.9072(2)	1.9126	1.9157	1.8930	<i>V</i> per atom	13.00	13.27	13.30	12.85
<i>d</i> Fe–O1	1.843(4)	1.8550	1.8813	1.8417	mean <i>d</i> Fe–O	1.8732	1.8754	1.9014	1.8732
<i>d</i> Fe–O1/ <i>d</i> Fe–O3	0.9663	0.9699	0.9820	0.9729	Fe–O3–Fe	124.6°	126.0°	122.9°	124.5°
<i>d</i> Cu–O2	1.9244(4)	1.9355	1.9473	1.9147	<i>d</i> Cu–O2	1.933(2)/1.934(2)	1.9365/1.9456	1.9413/1.9507	1.9267/1.9338
<i>d</i> Cu–O1	2.117(4)	2.1134	2.1197	2.0812	<i>d</i> Cu–O1	2.302(4)	2.4327	2.3883	2.3449
<i>d</i> Cu–O1/ <i>d</i> Cu–O2	1.1000	1.0919	1.0885	1.0870	<i>d</i> Cu–O1/ <i>d</i> Cu–O2	1.1906	1.2533	1.2273	1.2148
<i>d</i> Cu–Cu	3.407(4)	3.4435	3.5439	3.4297	<i>d</i> Cu–Cu	3.384(4)	3.2837	3.3506	3.3095
<i>d</i> Cu–Fe	3.960(3)	3.9684	4.0009	3.9229	<i>d</i> Cu–Fe	4.056(2)	4.1639	4.1337	4.0815

<sup>a</sup>The experimental data of YSr<sub>2</sub>Cu<sub>2</sub>FeO<sub>7.86</sub> (ICSD—11514) and YSr<sub>2</sub>Cu<sub>2</sub>FeO<sub>7.08</sub> (this work) are included for comparison. For the GGA + U method, a value of *U* = 4 eV is used for both Cu and Fe.

<sup>b</sup>Lattice parameters given in the setting for the S.G. *Ima2*. The unit cell metrics corresponding with the S.G. *Imma* (*Table 1*) is *a* (*Imma*) < > *c* (*Ima2*); *b* (*Imma*) < > *a* (*Ima2*); and *c* (*Imma*) < > *b* (*Ima2*).

to compare the band gap of YSr<sub>2</sub>Cu<sub>2</sub>FeO<sub>7.08</sub> with the DFT-calculated band gap.

**3.2. DFT Investigation of YSr<sub>2</sub>Cu<sub>2</sub>FeO<sub>8-δ</sub>.** **3.2.1. Metallic YSr<sub>2</sub>Cu<sub>2</sub>FeO<sub>8</sub> Phase.** Regardless of the constraints in comparing the experimental data of YSr<sub>2</sub>Cu<sub>2</sub>FeO<sub>7.85</sub> (*δ* = 0.15) and the idealized model YSr<sub>2</sub>Cu<sub>2</sub>FeO<sub>8</sub> (*δ* = 0), all of the utilized DFT methodologies reproduce the experimental lattice parameters and bond distances (**Table 2**), with small deviations ranging from a maximum of 4% (GGA + *U*) to a minimum of 0.2% (SCAN). The compression of the Fe octahedra (*d* Fe–O1/*d* Fe–O3 < 1) and the elongation of the Cu-square pyramid (*d* Cu–O1/*d* Cu–O2 > 1) along the *c*-axis are also well captured. There are, however, some subtle differences in the predicting capabilities of the four DFT methodologies. Both the GGA and GGA + *U* methods tend to produce larger lattice parameters, bonding distances (see for instance Fe–O1), and cell volume than the SCAN functional. For the YSr<sub>2</sub>Cu<sub>2</sub>FeO<sub>8-δ</sub> family, both *a* and *c* lattice parameters decrease with increasing oxygen content,<sup>23</sup> and hence the idealized stoichiometric compound YSr<sub>2</sub>Cu<sub>2</sub>FeO<sub>8</sub> should have a lower volume than the synthesized YSr<sub>2</sub>Cu<sub>2</sub>FeO<sub>7.85</sub>. In this respect, the SCAN functional offers superior performance in predicting such volume reduction.

The calculated magnetic moments and effective Bader charges (**Table 3**) differ among the different methodologies due to the distinct description of the transition-metal–oxygen bonding. The effective charge of all ions increases from the GGA to the GGA + *U*, as expected, due to the decreasing covalency of the Fe–O and Cu–O chemical bonds when correlation effects are taken into account. The poor electron localization in the GGA and SCAN approximations yields low magnetic moments on the transition-metal ions (0–0.2 and 2.7–3.0 μ<sub>B</sub> per Cu and Fe atom, respectively). Treating the correlation effects results in higher electron localization and larger calculated magnetic moments for Cu atoms (0.5 μ<sub>B</sub>) and Fe atoms (3.4 μ<sub>B</sub>). Neutron diffraction results and Mössbauer spectra of YSr<sub>2</sub>Cu<sub>2</sub>FeO<sub>7.85</sub> yielded a magnetic moment μ<sub>0</sub> (Fe) = 1.7–2 μ<sub>B</sub> per Fe atom that the authors attributed to Fe<sup>4+</sup> ion in low-spin configuration (*t*<sub>2g</sub><sup>4</sup>*e*<sub>g</sub><sup>0</sup>).<sup>24</sup> No magnetic moment was detected for Cu<sup>3+/2+</sup> ions. In this regard, although quantitative comparison of magnetic moments with experiments is complicated due to the observed Cu/Fe antisite mixing<sup>24,50</sup> and differences in the oxygen content, the GGA, and SCAN methodologies offer a more appropriate description than the GGA + *U*.

The three DFT approximations predict the metallic behavior of the YSr<sub>2</sub>Cu<sub>2</sub>FeO<sub>8</sub> oxide (see calculated DOS in **Figure 4**). Compared to the GGA method, the introduction of the *U* term produces a downshift of the occupied Cu/Fe-3*d* states. The *U* parameter keeps the 3*d* orbitals of Fe ions atomic-like, diminishing their hybridization with the 2*p* orbitals of the oxygen ions (less covalent Fe–O bonding). Although the Fe down-spin states are partially occupied under all approximations, the occupancy is the lowest for the GGA + *U* methodology, therefore resulting in the larger magnetic moment of 3.4 μ<sub>B</sub> per Fe atom, which is close to that expected for a high-spin Fe<sup>4+</sup> configuration (*t*<sub>2g</sub><sup>3</sup>*e*<sub>g</sub><sup>1</sup>), and deviates from the experimental observations.

**3.2.2. Insulating YSr<sub>2</sub>Cu<sub>2</sub>FeO<sub>7</sub> Phase.** **Figure 5a–c** shows the magnetic structures considered to model the idealized YSr<sub>2</sub>Cu<sub>2</sub>FeO<sub>7</sub> oxide. In the A-type structure, there are FM Cu/Fe in-plane interactions, while the planes order antiferromagnetically along the *a*-axis (tetragonal *c*-axis in YSr<sub>2</sub>Cu<sub>2</sub>FeO<sub>8</sub>). In

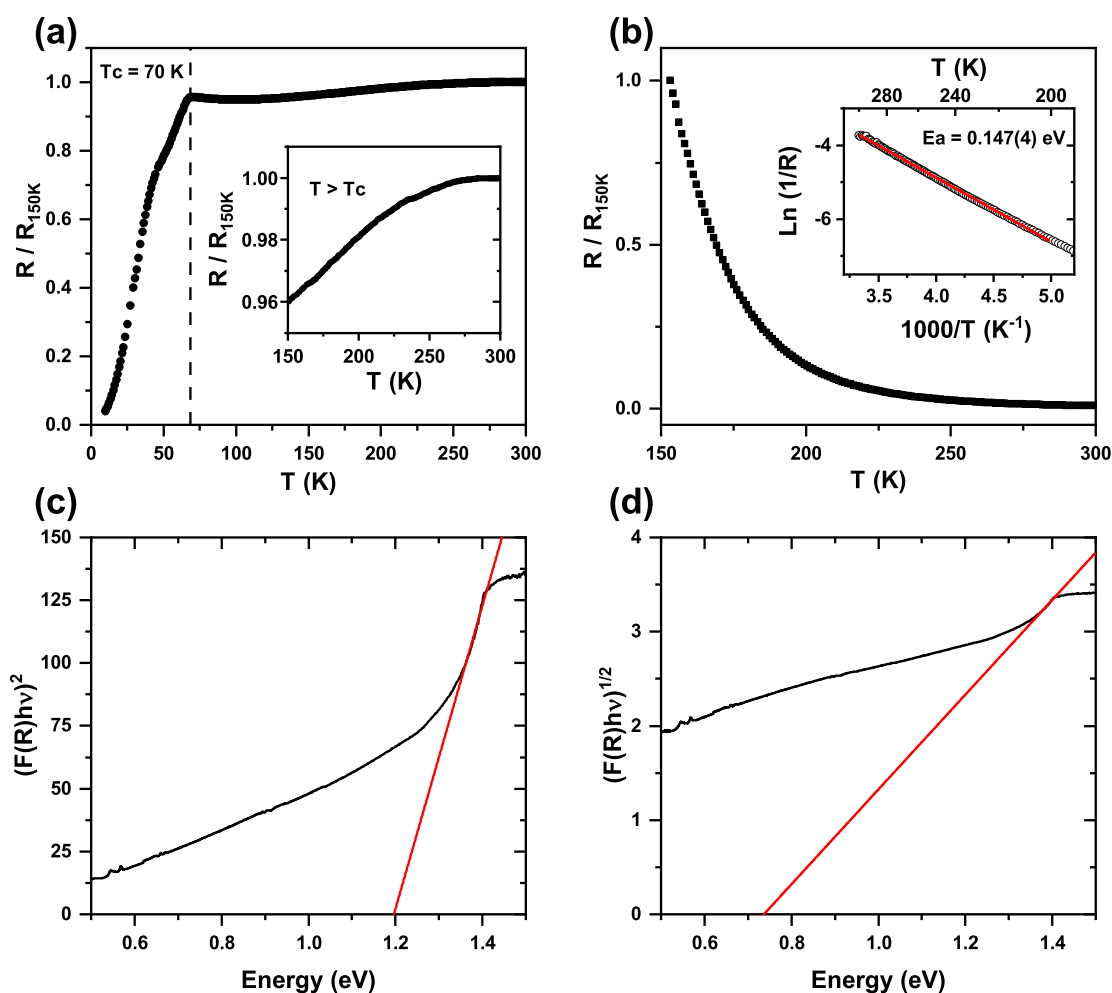


**Figure 3.** Normalized DC resistance for (a)  $\text{YSr}_2\text{Cu}_2\text{FeO}_{7.85}$  and (b)  $\text{YSr}_2\text{Cu}_2\text{FeO}_{7.08}$  oxides. The Arrhenius plot used for the determination of the activation energy ( $E_a$ ) is also shown in panel (b) as an inset. Tauc plot for  $\text{YSr}_2\text{Cu}_2\text{FeO}_{7.08}$  oxide considering direct (c) and indirect (d) allowed electronic transitions.

**Table 3.** Calculated Local Magnetic Moments  $\mu$  (in  $\mu_B$  per Atom) and Effective Bader Charges ( $Q$ ) for Idealized  $\text{YSr}_2\text{Cu}_2\text{FeO}_7$  and  $\text{YSr}_2\text{Cu}_2\text{FeO}_8$  Oxides<sup>a</sup>

	$\text{YSr}_2\text{Cu}_2\text{FeO}_8$			C-AFM $\text{YSr}_2\text{Cu}_2\text{FeO}_7$			
	GGA	GGA + $U$	SCAN	GGA	GGA + $U$	SCAN	
$Q$ (Fe)	1.796	1.881	1.930	$Q$ (Fe)	1.481	1.643	1.628
$Q$ (Cu)	1.073	1.090	1.157	$Q$ (Cu)	0.942	1.010	1.081
$Q$ (O1)	-1.158	-1.187	-1.228	$Q$ (O1)	-1.267	-1.324	-1.347
$Q$ (O2)	-1.187	-1.192	-1.232	$Q$ (O2)	-1.235	-1.260	-1.310
$Q$ (O3)	-1.125	-1.175	-1.175	$Q$ (O3)	-1.210	-1.297	-1.300
$\mu$ (Fe)	2.7	3.4	3.0	$\mu$ (Fe)	3.6	4.1	3.9
$\mu$ (Cu)	0.0	0.5	0.2	$\mu$ (Cu)	0.0	0.5	0.5
$\mu$ (O1)	0.1	0.0	0.1	$\mu$ (O1)	0.2	0.2	0.2
$\mu$ (O2)	0.0	0.1	0.0	$\mu$ (O2)	0.0	0.0	0.0
$\mu$ (O3)	0.2	0.1	0.1	$\mu$ (O3)	0.0	0.0	0.0

<sup>a</sup>Within the GGA +  $U$  method, a value of  $U = 4$  eV is used for both Cu and Fe.

the C-type, for each magnetic site, an in-plane AFM configuration between nearest-neighbor spins exists, while a FM configuration is set between the Fe and Cu planes. However, the sign reverses across the Y-layers due to the AFM direct exchange between  $\text{Cu}^{2+}$  cations at the face-confined pyramids. Within each  $(\text{CuO}_2\text{--SrO--FeO--SrO--CuO}_2)$  block, a C-type magnetic ordering is thus defined since the Cu/Fe magnetic moments can be grouped as chains along the

$a$ -axis (tetragonal  $c$ -axis in  $\text{YSr}_2\text{Cu}_2\text{FeO}_8$ ). The G-type presents the same AFM in-plane magnetic ordering of the C-type, but with AFM interactions between the Cu and Fe planes.

The four magnetic states tested to model  $\text{YSr}_2\text{Cu}_2\text{FeO}_7$  follow the energetic ordering: FM  $\sim$  A-AFM  $\gg$  G-AFM  $\sim$  C-AFM (Table 4). The large stabilization of the G and C-AFM types (about 0.4 eV/fu respective to the FM configuration) denotes strong in-plane Cu/Fe AFM interactions. On the

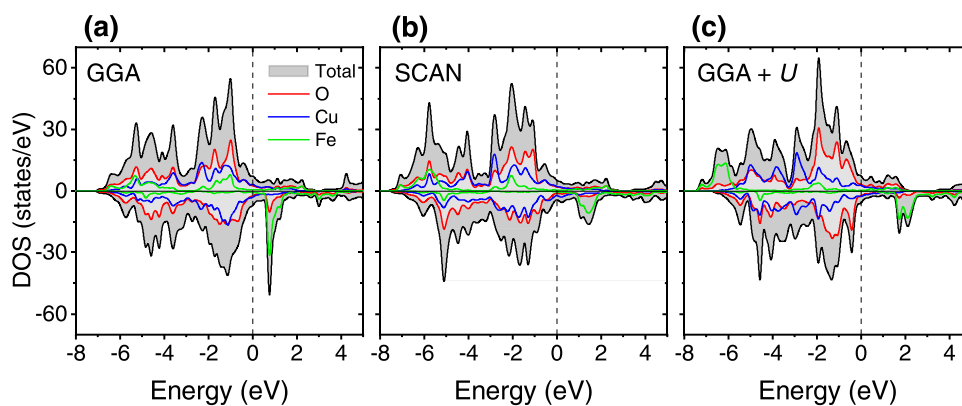


**Figure 4.** Calculated total and atom-projected density of states for  $\text{YSr}_2\text{Cu}_2\text{FeO}_8$ : (a) GGA functional, (b) SCAN functional, and (c) GGA +  $U$  method. The Fermi level is set as the zero of energy. Up-spin (or majority) and down-spin (or minority) contributions are shown in the upper and lower parts of the panels, respectively. Color code: total DOS in gray, Cu contribution in blue, Fe contribution in green, and O contribution in red. DOS units refer to the calculated cell.

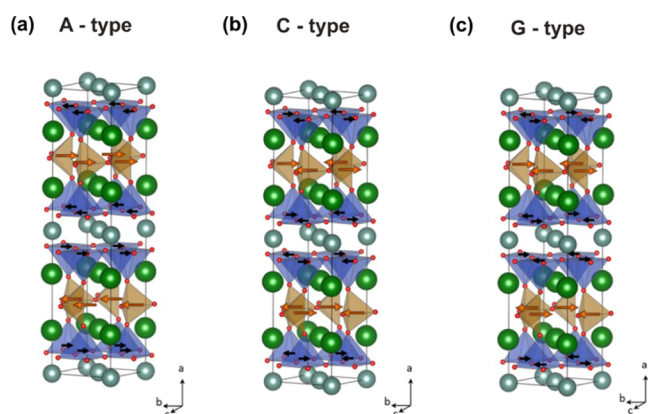


**Figure 5.** (a–c) Magnetic structures (C, G, A) used to simulate  $\text{YSr}_2\text{Cu}_2\text{FeO}_7$  (S.G. *Ima2*). Arrows indicate the spin orientation of the Fe and Cu atoms within the magnetic structure. Color code: Fe atoms in brown, Cu atoms in blue, Sr atoms in green, Y atoms in gray, and O atoms in red.

**Table 4.** Calculated Total-Energy Differences for Magnetic Configurations (Figure 5a–c) in  $\text{YSr}_2\text{Cu}_2\text{FeO}_7$  (in eV/fu)<sup>a</sup>

type	GGA	GGA + $U$	SCAN
A-AFM	0.020	0.020	−0.075
C-AFM	−0.248	−0.424	−0.414
G-AFM	−0.228	−0.375	−0.408

<sup>a</sup>The FM ordering is set as the zero of energy.

other hand, the small energy difference between G and C-AFM types, and between A-AFM and FM types, (5 meV/fu) suggests weak interplane magnetic interactions. The GGA, GGA +  $U$ , and SCAN methodologies predict the C-AFM to be the ground state, which has therefore been chosen to investigate the crystal and electronic structures of  $\text{YSr}_2\text{Cu}_2\text{FeO}_7$ .

Independently on the utilized functional, the optimization of the crystal structure of the idealized  $\text{YSr}_2\text{Cu}_2\text{FeO}_7$  oxide results in lattice parameters in reasonable agreement with the experimental values of  $\text{YSr}_2\text{Cu}_2\text{FeO}_{7.08}$  with errors below 2.1% (Table 2 and Figure S1). The GGA and GGA +  $U$  tend to overestimate the lattice parameters and TM–O distances, while the SCAN functional underestimates them. For the Fe environment, all of the approximations give a satisfactory

description of the average bond distances (errors below 0.7%), and even of the corrugation of the [FeO] layers, the SCAN results being the closest to the experimental values. However, the Cu–O square pyramidal environment is more elongated than the one experimentally observed ( $d_{\text{axial}}/d_{\text{equatorial}}$ ,  $d_{\text{Cu–O1}}/d_{\text{Cu–O2}}$  in Table 2). Since the hybridization of the Cu-apical oxygen plays a significant role in the electronic structure of YBCO-related oxides,<sup>51</sup> it is worth noting that the deviations in the Cu–O1 bond lengths are of 5.5% (GGA), 3.6% (GGA +  $U$ ), and 1.7% (SCAN). According to the major deviation in the Cu–O1 bond distance, the GGA fails to reproduce the semiconducting behavior of  $\text{YSr}_2\text{Cu}_2\text{FeO}_{7.08}$  (calculated DOS in Figure 6a) in clear disagreement with the experimental observations (Figure 3b).

While the GGA incorrectly predicts the metallic behavior for the ground state of idealized  $\text{YSr}_2\text{Cu}_2\text{FeO}_7$ , a band gap of 0.85 eV opens in the GGA +  $U$  ( $U_{\text{Cu}}$  and  $U_{\text{Fe}} = 4$  eV), and noteworthy, a near band gap of 0.63 eV is obtained using the SCAN functional (Figure 6). Compared to the  $\text{YSr}_2\text{Cu}_2\text{FeO}_8$  phase, in both SCAN and GGA +  $U$ , the effective charge of the TMs decreases (Table 3), and the TM–O distances increase (Table 2), in agreement with the lower formal oxidation states of  $\text{Fe}^{3+}$  and  $\text{Cu}^{2+}$  in  $\text{YSr}_2\text{Cu}_2\text{FeO}_7$ . The effective charge on oxygen ions increases, approaching the oxide ion  $\text{O}^{2-}$ . SCAN and GGA +  $U$  methods predict nearly the same calculated magnetic moments for TM ions:  $\mu(\text{Cu}) = 0.5 \mu_{\text{B}}$  per atom and  $\mu(\text{Fe}) \sim 4 \mu_{\text{B}}$  per atom. The magnetic moment of the Cu ions is in good agreement with the experimental values reported in similar  $\text{Cu}^{2+}$  compounds.<sup>52,53</sup> The magnetic moment on Fe ions suggests a high-spin  $\text{Fe}^{3+}$  configuration ( $e^2t_2^3$ , magnetic moment of the free ion  $\mu_0 = 5.0 \mu_{\text{B}}$ ). It is worth to note that magnetic moment values between 3 and 4  $\mu_{\text{B}}$  per atom have been experimentally observed in other complex  $\text{Fe}^{3+}$ -tetrahedral oxides.<sup>54,55</sup> On the other hand, the Fe–O and Cu–O covalencies bring an appreciable spin moment of  $\sim 0.2 \mu_{\text{B}}$  in the shared O1 site. As observed in the atom-projected density of states (Figure 6c), the  $U$  term shifts the TM-3d states to lower energies; yet, there is a good hybridization of TM-3d to O-2p states (see band at −6 eV). In summary, for the insulating compound, SCAN offers very similar results to the GGA +  $U$  in terms of band-gap and magnetic moments, although there are clear differences in the shape and nature of the states at the Fermi level. To further analyze the appropriateness of the SCAN vs. the GGA +  $U$  method, in a

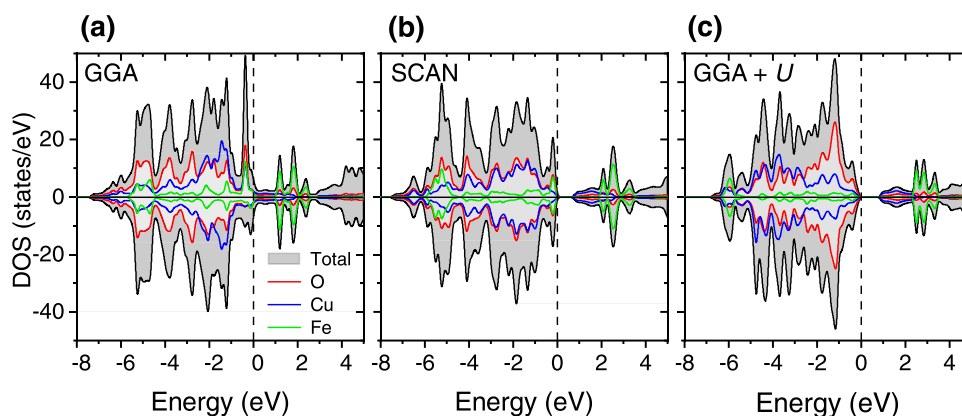


**Figure 6.** Calculated total and atom-projected density of states (DOS) for the ground-state C-magnetic structure of the idealized  $\text{YSr}_2\text{Cu}_2\text{FeO}_7$ : (a) GGA functional, (b) SCAN functional, and (c) GGA +  $U$  method. The Fermi level is set as the zero of energy. Up-spin (or majority) and down-spin (or minority) contributions are shown. Color code: total black, Cu contribution in blue, Fe contribution in green, and O contribution in red. DOS units refer to the calculated cell.

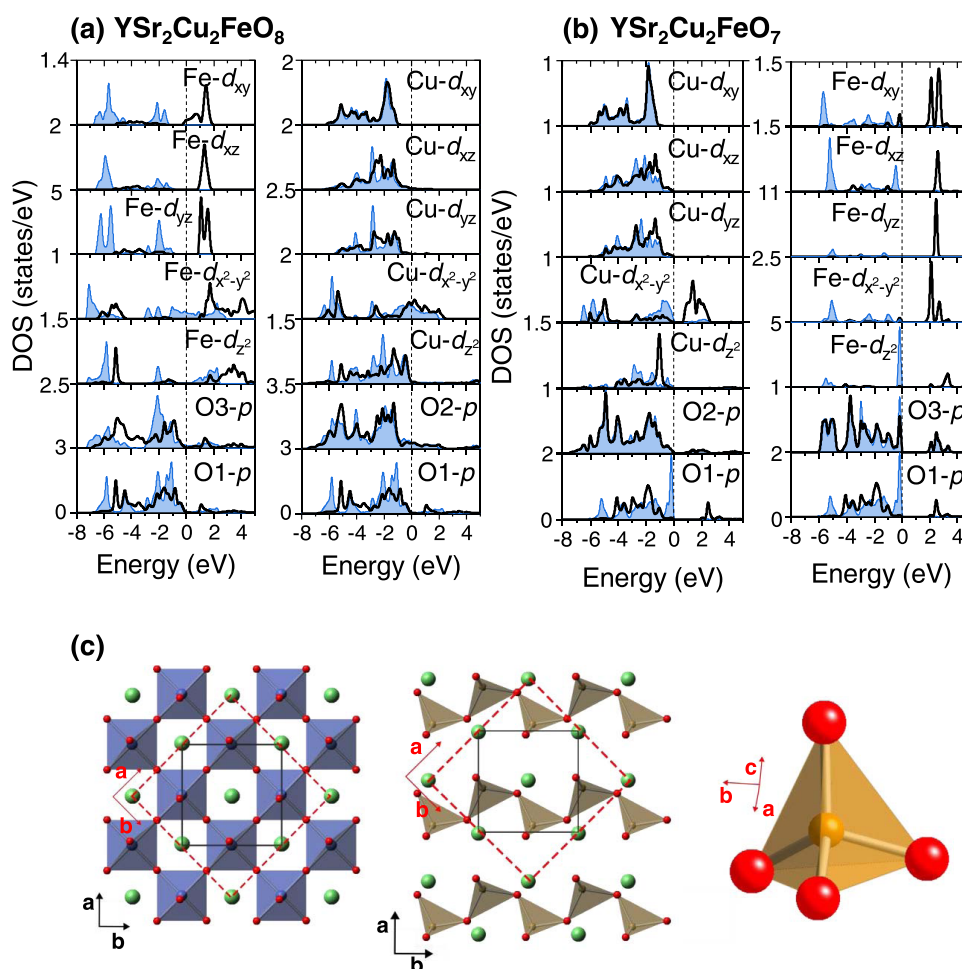


**Figure 7.** Orbital-projected density of states within the SCAN functional for (a) idealized  $\text{YSr}_2\text{Cu}_2\text{FeO}_8$  showing the Fe-3d, O3-2p and O1-2p and Cu-3d, O2-2p, and O1-2p orbitals, and (b) idealized  $\text{YSr}_2\text{Cu}_2\text{FeO}_7$  showing the Cu-3d, O2-2p and O1-2p and Fe-3d, O3-2p, and O1-2p orbital contribution. Color code: up-spin (or majority) in blue and down-spin (or minority) in black. (c) Crystallographic cell used for the orbital-projected DOS of  $\text{YSr}_2\text{Cu}_2\text{FeO}_7$  (in red) and its relation to the crystal setting in the  $Ima2$  S.G. (in black).

first approximation, the calculated DOS could be qualitatively compared with experimental photoelectron spectroscopy (PES). It is however important to point out that such comparison neglects the excitation aspects, which can be taken

into account by quasi-particle calculations in the GW approach.<sup>56</sup>

For the sake of completeness, the relation between the electronic properties and the magnetic structure of  $\text{YSr}_2\text{Cu}_2\text{FeO}_7$  is analyzed within the SCAN and GGA +  $U$

methods (Figure S2). Once more, both DFT approximations yield the same results in terms of the insulating/metallic behavior. The calculated DOS for the G magnetic structure, with in-plane Cu/Fe AFR interactions, corresponds to an insulating compound with the same band gap of the C-magnetic structure (0.63 eV in SCAN, 0.85 eV in GGA+  $U$ ). The FR and A magnetic structures, with in-plane Cu/Fe FR interactions, generate metallic properties. These results reveal that, for the idealized  $\text{YSr}_2\text{Cu}_2\text{FeO}_7$ , the insulating character couples to the in-plane AFM Cu/Fe ordering.

**3.2.3. On the Metal-to-Insulating Transition in the  $\text{YSr}_2\text{Cu}_2\text{FeO}_{8-\delta}$  ( $0 < \delta < 1$ ) Family.** The above results highlight that the SCAN functional reproduces the metal and the insulating character of  $\text{YSr}_2\text{Cu}_2\text{FeO}_8$  and  $\text{YSr}_2\text{Cu}_2\text{FeO}_7$  compounds, respectively. The orbital-projected DOS (Figure 7) adds more insights into the comprehensive interpretation of the chemical bonding and the evolution of the electronic properties as a function of the  $\delta$  value. Starting with the metallic  $\text{YSr}_2\text{Cu}_2\text{FeO}_8$ , in the Fe octahedra, the hybridization of  $\text{O}3(2p)\text{-Fe}(3d_{x^2-y^2})$  and  $\text{O}1(2p)\text{-Fe}(3d_z^2)$  produces the lower energy band  $\sigma\text{-O}(p)\text{-Fe}(e_g)$  and the upper energy band  $\sigma^*\text{-O}(p)\text{-Fe}(e_g)$ . As observed in Figure 7a, the occupation of the bonding sigma band occurs in both spin channels, with the Fermi level crossing the  $3d_{x^2-y^2}$  majority spin orbital. The  $\Pi$   $\text{O}(2p)\text{-Fe}(3t_{2g})$  bands are fully occupied in the up-spin channel, but also show some occupancy in the down-spin channel. As deduced from the calculated magnetic moments, the  $3d$ -Fe orbitals filling does not correspond to either LS- $\text{Fe}^{4+}$  ( $t_{2g}^4 e_g^0$ ) or HS- $\text{Fe}^{4+}$  ( $t_{2g}^3 e_g^1$ ), but to an itinerant character where every  $3d$  orbital contributes to the magnetic moment, in agreement with the metallic properties of the oxide. For the Cu- $3d$  states, the crystal field splitting of the Cu-O square pyramidal environment lifts the degeneracy of the Cu- $e_g$  orbitals to the lower-lying  $3d_z^2$  and higher-lying  $3d_{x^2-y^2}$  orbitals. The strong hybridization  $\text{O}2(2p)\text{-Cu}(3d_{x^2-y^2})$  produces a wide band that is partially filled in both spin channels, yielding a low net spin of  $0.3 \mu_B$ . The Fermi level lies in the band constructed mainly from the Cu- $3d_{x^2-y^2}$  and O2- $2p$  orbitals and in a minor extent in the band constructed from Fe- $3d_{x^2-y^2}$  and O3- $2p$  orbitals. Therefore, these bands have the largest implication in the electronic properties of the  $\text{YSr}_2\text{Cu}_2\text{FeO}_{8-\delta}$  family.

Upon vacancies incorporation in  $\text{YSr}_2\text{Cu}_2\text{FeO}_8$  (Figure 7a) to form  $\text{YSr}_2\text{Cu}_2\text{FeO}_7$  (Figure 7b), according to the Fermi-level displacement, electron filling occurs in the Cu- $3d_{x^2-y^2}$  derived band. Since in  $\text{YSr}_2\text{Cu}_2\text{FeO}_7$  the Cu ions have the nominal valence of 2+, and hence a nominal  $d^9$  state, there are fully occupied  $t_{2g}$  orbitals and  $d_z^2$  orbitals, while the  $d_{x^2-y^2}$  orbital remains half-filled yielding a low net spin of  $0.5 \mu_B$ . The energy gap opens between the occupied and the unoccupied Cu- $3d_{x^2-y^2}$  orbitals. On the other hand, the analysis of the Fe- $3d$  states upon electron doping of  $\text{YSr}_2\text{Cu}_2\text{FeO}_8$  is more complicated, since the coordination around the Fe atoms changes from octahedral in  $\text{YSr}_2\text{Cu}_2\text{FeO}_8$  to tetrahedral in  $\text{YSr}_2\text{Cu}_2\text{FeO}_7$ . According to crystal field theory, in the tetrahedral field, the Fe- $3d$  orbitals split into two manifolds, a lower one with two levels and an upper one with three levels (these would be of  $e$  and  $t_2$  character respectively, if the local symmetry were perfectly tetrahedral). This is not observed in Figure 7b due to the orientation of the Fe tetrahedra relative to the crystallographic cell axes utilized for the orbital-projected DOS (Figure 7c). Nevertheless, for all of the Fe- $3d$  states, the up-spin channel is fully occupied and the down-spin channel is

almost empty, the energy separation between up and down-spin channels being rather large. This electron density localization leads to the aforementioned high-spin  $\text{Fe}^{3+}$  configuration.

In summary, the results of the SCAN methodology indicate that in the  $\text{YSr}_2\text{Cu}_2\text{FeO}_{8-\delta}$  family, the lowering of the oxygen content drives the metal-to-insulating transition by electron doping. A reduction in the oxygen content (higher  $\delta$  value) results in a decrease in the nominal valence of Cu/Fe ions, and hence in the filling of the Cu/Fe- $3d_{x^2-y^2}$  states. This picture is fully consistent with the well-documented importance of filling control in the electronic structure of high  $T_c$  cuprates, a typical example being the insulating to metal transition in  $\text{La}_{2-x}\text{Sr}_x\text{CuO}_4$  induced by hole doping ( $x = 0$  metallic).<sup>18,57</sup>

Remarkably, the SCAN functional offers a feasible interpretation of the metal-to-insulating transition in the  $\text{YSr}_2\text{Cu}_2\text{FeO}_{8-\delta}$  family, when looking at the idealized compounds with  $\delta = 0$  and 1. However, in addition to distinct oxygen contents ( $\delta$  values), the synthesized compounds  $\text{YSr}_2\text{Cu}_2\text{FeO}_{7.86}$  ( $\delta = 0.14$ ) and  $\text{YSr}_2\text{Cu}_2\text{FeO}_{7.08}$  ( $\delta = 0.92$ ) show antisite disorder, with a Cu/Fe mixing close to 15% (see Table 1 and ref 24). As noted by different authors,<sup>22-24,58,59</sup> the mutual substitution of Cu and Fe depends on the annealing history/oxygen content. The simulation of the random distribution of the antisite defects that occurs in the real materials requires the utilization of the special quasi-random structures (SQS) approach,<sup>60</sup> which is out of the scope of this work. The antisite disorder could perturb the AFM in-plane ordering that, as discussed above, is critically linked to the insulating behavior of the investigated compounds with the lowest oxygen contents ( $\delta \sim 0$ ). It is foreseeable that the concentration and location of both oxygen vacancies and antisite defects drastically influence the magnetic and electronic properties of the  $\text{YSr}_2\text{Cu}_2\text{FeO}_{8-\delta}$  family. This is in agreement with the observed dependence between the property and the synthetic history of the materials.

## 4. CONCLUSIONS

The precise modeling of the ground-state properties in complex oxides that contain more than one type of TM ions remains challenging, especially with the irruption of correlated oxides as functional materials. In this work, we have examined the capabilities of different DFT methodologies (GGA, GGA +  $U$ , SCAN) to model the crystal structure and the electronic and magnetic properties of  $\text{YSr}_2\text{Cu}_2\text{FeO}_{8-\delta}$  compounds in which the oxygen content in the  $\text{FeO}_{2-\delta}$  layers drives the average oxidation states of both Fe and Cu cations, thereby determining the electrical properties. We have found that the SCAN and GGA methodologies are valid to simulate the metallic properties of the oxide with the highest oxygen content of the family ( $\delta = 0$ , idealized- $\text{YSr}_2\text{Cu}_2\text{FeO}_8$ ) and the itinerant character of its bonding electrons. Introducing the  $U$  term (GGA +  $U$ ) results in excessive electron localization and large magnetic moments that deviate from the experimental observations, therefore discarding this methodology for property prediction in the metallic phases of the  $\text{YSr}_2\text{Cu}_2\text{FeO}_{8-\delta}$  system. Contrariwise, the insulating character of the compound with the lowest oxygen content ( $\delta = 1$ , idealized- $\text{YSr}_2\text{Cu}_2\text{FeO}_7$ ) is well captured when electron correlations are treated by the  $U$  parameter using the GGA +  $U$  approximation. Importantly, the results point out that the SCAN functional also offers a good platform to investigate these insulating compounds. These results render the SCAN

functional as the only one well suited, among the utilized methodologies, to investigate the basic electronic properties across the  $\text{YSr}_2\text{Cu}_2\text{FeO}_{8-\delta}$  series. It should be noted that, together with the lack of an adjustable  $U$  parameter, other benefits of the SCAN functional are the affordable computational cost and the transferability of results among different works. Yet, a severe limiting factor for the DFT investigation of the  $\text{YSr}_2\text{Cu}_2\text{FeO}_{8-\delta}$  family resides in the need of complex crystallographic models to take into account the antisite Cu/Fe disorder and the fractional occupancies of the O3 site that occur in the synthesized materials.

## ■ ASSOCIATED CONTENT

### SI Supporting Information

The Supporting Information is available free of charge at <https://pubs.acs.org/doi/10.1021/acs.inorgchem.2c03475>.

Calculated lattice parameters and density of states for the A-AFM, G-AFM, and FM magnetic structures of  $\text{YSr}_2\text{Cu}_2\text{FeO}_7$  (PDF)

## ■ AUTHOR INFORMATION

### Corresponding Author

M. Elena Arroyo-de Dompablo – Departamento de Química Inorgánica, Universidad Complutense de Madrid, 28040 Madrid, Spain; [orcid.org/0000-0001-5249-3562](https://orcid.org/0000-0001-5249-3562); Email: [e.arroyo@quim.ucm.es](mailto:e.arroyo@quim.ucm.es)

### Authors

Marianela Gómez-Toledo – Departamento de Química Inorgánica, Universidad Complutense de Madrid, 28040 Madrid, Spain; [orcid.org/0000-0001-5594-4146](https://orcid.org/0000-0001-5594-4146)

Sara A. López-Paz – Departamento de Química Inorgánica, Universidad Complutense de Madrid, 28040 Madrid, Spain; Department of Quantum Matter Physics, University of Geneva, CH-1211 Geneva, Switzerland

Susana García-Martín – Departamento de Química Inorgánica, Universidad Complutense de Madrid, 28040 Madrid, Spain; [orcid.org/0000-0003-0729-4892](https://orcid.org/0000-0003-0729-4892)

Complete contact information is available at: <https://pubs.acs.org/doi/10.1021/acs.inorgchem.2c03475>

### Author Contributions

M.G.-T. performed the DFT calculations including the data preparation/analysis, tables, and graphical representations. She performed the spectroscopy measurements, interpretation, and graphics, and she also contributed in writing the original draft of the manuscript. S.A.L.-P. conducted the experimental research comprising the synthesis and structural and electrical characterization of the materials. S.G.-M. led the experimental project administration. M.E.A.-d.D. directed the computational investigation, led the computational project administration, and wrote the draft of the manuscript. All authors contributed in the discussion and writing of the final version of the manuscript. All authors have given approval to the final version of the manuscript.

### Notes

The authors declare no competing financial interest.

## ■ ACKNOWLEDGMENTS

The authors thank MCIN/AEI/10.13039/501100011033 and “NextGenerationEU”/PRTR for funding the Projects PID2019-106662RB-C44 and TED2021-130452B-C21.

M.E.A.-d.D. and M.G.-T. acknowledge funding for computational research and spectroscopy measurements from Universidad Complutense de Madrid (FEI-EU-22-01-4129585). M.G.-T. thanks Comunidad de Madrid for contract (PEJ-2020-AI/IND-18065) of the program “Ayudas para la contratación de Ayudantes de Investigación y Técnicos de Laboratorio”. The authors acknowledge Dr. Clemens Ritter for the neutron diffraction measurements and the ILL for beam time allocation in the D2B instrument under the experiment code 5-23-705. Data are available from ILL at DOI: 10.5291/ILL-DATA.5-23-705. The authors are grateful to R. González-Prieto for his assistance in the Reflectance Diffuse Spectroscopy measurements.

## ■ REFERENCES

- (1) Irvine, J.; Rupp, J. L. M.; Liu, G.; Xu, X.; Haile, S.; Qian, X.; Snyder, A.; Freer, R.; Ekren, D.; Skinner, S.; Celikbilek, O.; Chen, S.; Tao, S.; Shin, T. H.; O’Hayre, R.; Huang, J.; Duan, C.; Papac, M.; Li, S.; Celorrio, V.; Russell, A.; Hayden, B.; Nolan, H.; Huang, X.; Wang, G.; Metcalfe, I.; Neagu, D.; Martin, S. G. Roadmap on inorganic perovskites for energy applications. *J. Phys.: Energy* **2021**, *3*, No. 031502.
- (2) Hohenberg, P.; Kohn, W. Inhomogeneous electron gas. *Phys. Rev. B: Condens. Matter Mater. Phys.* **1964**, *136*, B864–B871.
- (3) Kohn, W.; Sham, L. J. Self-consistent equations including exchange and correlation effects. *Phys. Rev.* **1965**, *140*, A1133.
- (4) Perdew, J. P. Generalized gradient approximations for exchange and correlation - a look backward and forward. *Phys. B* **1991**, *172*, 1–6.
- (5) Perdew, J. P.; Yue, W. Accurate and simple density functional for the electronic exchange energy - Generalized Gradient Approximation. *Phys. Rev. B: Condens. Matter Mater. Phys.* **1986**, *33*, 8800–8802.
- (6) Piskunov, S.; Heifets, E.; Eglitis, R. I.; Borstel, G. Bulk properties and electronic structure of  $\text{SrTiO}_3$ ,  $\text{BaTiO}_3$ ,  $\text{PbTiO}_3$  perovskites: an ab initio HF/DFT study. *Comput. Mater. Sci.* **2004**, *29*, 165–178.
- (7) Eng, H. W.; Barnes, P. W.; Auer, B. M.; Woodward, P. M. Investigations of the electronic structure of  $d^0$  transition metal oxides belonging to the perovskite family. *J. Solid State Chem.* **2003**, *175*, 94–109.
- (8) Oja, R.; Tyunina, M.; Yao, L.; Pinomaa, T.; Kocourek, T.; Dejneka, A.; Stupakov, O.; Jelinek, M.; Trepakov, V.; van Dijken, S.; Nieminen, R. M.  $d^0$  Ferromagnetic Interface between Nonmagnetic Perovskites. *Phys. Rev. Lett.* **2012**, *109*, No. 127207.
- (9) Bilc, D. I.; Orlando, R.; Shaltaf, R.; Rignanese, G. M.; Iniguez, J.; Ghosez, P. Hybrid exchange-correlation functional for accurate prediction of the electronic and structural properties of ferroelectric oxides. *Phys. Rev. B: Condens. Matter Mater. Phys.* **2008**, *77*, No. 165107.
- (10) Anisimov, V. I.; Zaanen, J.; Andersen, O. K. Band Theory and Mott Insulators - Hubbard-U Instead of Stoner-I. *Phys. Rev. B: Condens. Matter Mater. Phys.* **1991**, *44*, 943–954.
- (11) Zhou, F.; Marianetti, C. A.; Cococcioni, M.; Morgan, D.; Ceder, G. Phase separation in  $\text{Li}_x\text{FePO}_4$  induced by correlation effects. *Phys. Rev. B: Condens. Matter Mater. Phys.* **2004**, *69*, No. 201101.
- (12) Ganduglia-Pirovano, M. V.; Hofmann, A.; Sauer, J. Oxygen vacancies in transition metal and rare earth oxides: Current state of understanding and remaining challenges. *Surf. Sci. Rep.* **2007**, *62*, 219.
- (13) Wang, L.; Maxisch, T.; Ceder, G. Oxidation energies of transition metal oxides within the GGA+ $U$  framework. *Phys. Rev. B: Condens. Matter Mater. Phys.* **2006**, *73*, No. 195107.
- (14) Anisimov, V. I.; Aryasetiawan, F.; Lichtenstein, A. I. First-principles calculations of the electronic structure and spectra of strongly correlated systems: The LDA+ $U$  method. *J. Phys.: Condens. Matter* **1997**, *9*, 767–808.

- (15) Sun, J.; Ruzsinszky, A.; Perdew, J. P. Strongly Constrained and Appropriately Normed Semilocal Density Functional. *Phys. Rev. Lett.* **2015**, *115*, No. 036402.
- (16) Hinuma, Y.; Hayashi, H.; Kumagai, Y.; Tanaka, I.; Oba, F. Comparison of approximations in density functional theory calculations: Energetics and structure of binary oxides. *Phys. Rev. B: Condens. Matter Mater. Phys.* **2017**, *96*, No. 094102.
- (17) Kitchaev, D. A.; Peng, H.; Liu, Y.; Sun, J.; Perdew, J. P.; Ceder, G. Energetics of MnO<sub>2</sub> polymorphs in density functional theory. *Phys. Rev. B: Condens. Matter Mater. Phys.* **2016**, *93*, No. 045132.
- (18) Furness, J. W.; Zhang, Y.; Lane, C.; Buda, I. G.; Barbiellini, B.; Markiewicz, R. S.; Bansil, A.; Sun, J. An accurate first-principles treatment of doping-dependent electronic structure of high-temperature cuprate superconductors. *Commun. Phys.* **2018**, *1*, No. 11.
- (19) Kaczkowski, J.; Pugaczowa-Michalska, M.; Płowaś-Korus, I. Isovalent cation ordering in Bi-based double perovskites: A density functional analysis. *J. Magn. Magn. Mater.* **2022**, *548*, No. 168984.
- (20) Iglesias, L.; Bibes, M.; Varignon, J. First-principles study of electron and hole doping effects in perovskite nickelates. *Phys. Rev. B: Condens. Matter Mater. Phys.* **2021**, *104*, No. 035123.
- (21) Varignon, J.; Bibes, M.; Zunger, A. Mott gapping in 3d ABO<sub>3</sub> perovskites without Mott-Hubbard interelectronic repulsion energy *U*. *Phys. Rev. B: Condens. Matter Mater. Phys.* **2019**, *100*, No. 035119.
- (22) Shimoyama, J.; Otschi, K.; Hinouchi, T.; Kishio, K. Discovery of superconductivity in Fe-based cuprates. *Phys. C* **2000**, *341–348*, 563–564.
- (23) Mochiku, T.; Nakano, Y.; Hoshikawa, A.; Sato, S.; Oikawa, K.; Ishigaki, T.; Kamiyama, T.; Kadowaki, K.; Hirata, K. Superstructure in Sr<sub>2</sub>YCu<sub>2</sub>FeO<sub>6+δ</sub>. *Phys. C* **2004**, *412–414*, 115–119.
- (24) López-Paz, S. A.; Martínez de Irujo-Labalde, X.; Sanchez-Marcos, J.; Ritter, C.; Moran, E.; Alario-Franco, M. A. Soft Magnetic Switching in a FeSr<sub>2</sub>YCu<sub>2</sub>O<sub>7.85</sub> Superconductor with Unusually High Iron Valence. *Inorg. Chem.* **2019**, *58*, 12809–12814.
- (25) Mochiku, T.; Hata, Y.; Yamaguchi, K.; Tsuchiya, Y.; Hoshikawa, A.; Iwase, K.; Sulistyanintyas, D.; Ishigaki, T.; Yasuoka, H.; Hirata, K. Annealing effect on structure and superconductivity in FeSr<sub>2</sub>YCu<sub>2</sub>O<sub>6+δ</sub> magnetic superconductor. *Phys. Procedia* **2012**, *45*, 73–76.
- (26) Sansom, J. E. H.; Kendrick, E.; Rudge-Pickard, H. A.; Islam, M. S.; Wright, A. J.; Slater, P. R. Synthesis and characterisation of the perovskite-related cuprate phases YSr<sub>2</sub>Cu<sub>2</sub>MO<sub>7+y</sub> (M = Co, Fe) for potential use as solid oxide fuel cell cathode materials. *J. Mater. Chem.* **2005**, *15*, 2321–2327.
- (27) López-Paz, S. A.; Marin-Gamero, R.; Martínez de Irujo-Labalde, X.; Sanchez-Marcos, J.; Perez-Coll, D.; Franco, M. A. A. Y.; Garcia-Martin, S. YBaCuO-type perovskites as potential air electrodes for SOFCs. The case of YSr<sub>2</sub>Cu<sub>2</sub>FeO<sub>7+δ</sub>. *J. Mater. Chem. A* **2021**, *9*, 8554–8560.
- (28) Mochiku, T.; Nakano, Y.; Oikawa, K.; Kamiyama, T.; Fujii, H.; Hata, Y.; Suzuki, I.; Takeya, I.; Kadowaki, K.; Hirata, K. Atomic ordering in FeSr<sub>2</sub>LnCu<sub>2</sub>O<sub>6+δ</sub> system (Ln = Nd, Y and Er). *Phys. C* **2003**, *400*, 43–52.
- (29) Pissas, M.; Kallias, G.; Moraitakis, E.; Niarchos, D.; Simopoulos, A. Site occupancy of Fe in the oxygen-saturated YSr<sub>2</sub>Cu<sub>3-x</sub>Fe<sub>x</sub>O<sub>y</sub> compound for x=0.25 up to 1. *Phys. C* **1994**, *234*, 127–136.
- (30) Lopez-Paz, S. A.; Sari, D. P.; Hillier, A. D.; Alario-Franco, M. A. Coexistence of magnetism and superconductivity in the iron containing FeSr<sub>2</sub>YCu<sub>2</sub>O<sub>7.57</sub> cuprate as studied by  $\mu$ -SR. *AIP Adv.* **2021**, *11*, No. 015011.
- (31) Rodriguez-Carvajal, J. Recent advances in magnetic structure determination by neutron powder diffraction. *Physica B* **1993**, *192*, 55–69.
- (32) Kubelka, P.; Munk, F. A. Contribution to the Optics of Pigments. *Z. Technol. Phys.* **1931**, *12*, 593–599.
- (33) Tauc, J.; Grigorovici, R.; Vancu, A. Optical Properties And Electronic Structure of Amorphous Germanium. *Phys. Status Solidi B* **1966**, *15*, 627–637.
- (34) Kresse, G.; Furthmüller, J. Efficient iterative schemes for ab initio total-energy calculations using a plane-wave basis set. *Phys. Rev. B* **1996**, *54*, 11169.
- (35) Kresse, G.; Joubert, D. From ultrasoft pseudopotentials to the projector augmented-wave method. *Phys. Rev. B* **1999**, *59*, 1758.
- (36) Blöchl, P. E. Projector augmented-wave method. *Phys. Rev. B* **1994**, *50*, 17953.
- (37) Perdew, J. P.; Burke, K.; Ernzerhof, M. Generalized gradient approximation made simple. *Phys. Rev. Lett.* **1996**, *77*, 3865–3868.
- (38) Blöchl, P. E.; Jepsen, O.; Andersen, O. K. Improved tetrahedron method for Brillouin-zone integrations. *Phys. Rev. B: Condens. Matter Mater. Phys.* **1994**, *49*, 16223–16233.
- (39) Dudarev, S. L.; Botton, G. A.; Savrasov, S. Y.; Szotek, Z.; Temmerman, W. M.; Sutton, A. P. Electronic structure and elastic properties of strongly correlated metal oxides from first principles: LSDA+*U*, SIC-LSDA and EELS study of UO<sub>2</sub> and NiO. *Phys. Status Solidi A* **1998**, *166*, 429–443.
- (40) Arroyo y de Dompablo, M. E.; Lee, Y.-L.; Morgan, D. First Principles Investigation of Oxygen Vacancies in Columbite MNb<sub>2</sub>O<sub>6</sub> (NI = Mn, Fe, Co, Ni, Cu). *Chem. Mater.* **2010**, *22*, 906–913.
- (41) Ritzmann, A. M.; Dieterich, J. M.; Carter, E. A. Density functional theory plus *U* analysis of the electronic structure and defect chemistry of LSCF (La<sub>0.5</sub>Sr<sub>0.5</sub>Co<sub>0.25</sub>Fe<sub>0.75</sub>O<sub>3-δ</sub>). *Phys. Chem. Chem. Phys.* **2016**, *18*, 12260–12269.
- (42) Jain, A.; Shyue Ping, O.; Hautier, G.; Chen, W.; Richards, W. D.; Dacek, S.; Cholia, S.; Gunter, D.; Skinner, D.; Ceder, G.; Persson, K. A. Commentary: The Materials Project: A materials genome approach to accelerating materials innovation. *APL Mater.* **2013**, *1*, No. 011002.
- (43) Bader, R. F. W. *Atoms in Molecules: A Quantum Theory*; Oxford University Press: Oxford, U.K., 1990.
- (44) Henkelman, G.; Arnaldsson, A.; Jónsson, H. A fast and robust algorithm for Bader decomposition of charge density. *Comput. Mater. Sci.* **2006**, *36*, 354–360.
- (45) Ong, S. P.; Richards, W. D.; Jain, A.; Hautier, G.; Kocher, M.; Cholia, S.; Gunter, D.; Chevrier, V. L.; Persson, K. A.; Ceder, G. Python Materials Genomics (pymatgen): A robust, open-source python library for materials analysis. *Comput. Mater. Sci.* **2013**, *68*, 314–319.
- (46) Roth, G.; Adelman, P.; Heger, G.; Knitter, R.; Wolf, T. The crystal-structure of RESr<sub>2</sub>GaCu<sub>2</sub>O<sub>7</sub>. *J. Phys. I* **1991**, *1*, 721–741.
- (47) Dolgonos, A.; Mason, T. O.; Poeppelmeier, K. R. Direct optical band gap measurement in polycrystalline semiconductors: A critical look at the Tauc method. *J. Solid State Chem.* **2016**, *240*, 43–48.
- (48) Wu, J.; Walukiewicz, W.; Yu, K. M.; Ager, J. W.; Haller, E. E.; Lu, H.; Schaff, W. J.; Saito, Y.; Nanishi, Y. Unusual properties of the fundamental band gap of InN. *Appl. Phys. Lett.* **2002**, *80*, 3967–3969.
- (49) Kobayashi, H.; Mori, T.; Namba, K.; Nakato, Y. New method for determination of energy distribution of surface states in the semiconductor band-gap: XPS measurements under biases. *Solid State Commun.* **1994**, *92*, 249–254.
- (50) Pissas, M.; Kallias, G.; Simopoulos, A.; Niarchos, D.; Sonntag, R. Neutron diffraction study of the deoxygenated YSr<sub>2</sub>Cu<sub>3-x</sub>Fe<sub>x</sub>O<sub>6+y</sub> (x = 0.8 and 1) compound. *Phys. B* **1998**, *253*, 1–9.
- (51) Ohta, Y.; Tohyama, T.; Maekawa, S. Transition-temperature in copper-oxide superconductors correlated with energy-level of apical oxygen. *Phys. C* **1990**, *166*, 385–387.
- (52) Tranquada, J. M.; Moudden, A. H.; Goldman, A. I.; Zolliker, P.; Cox, D. E.; Shirane, G.; Sinha, S. K.; Vaknin, D.; Johnston, D. C.; Alvarez, M. S.; Jacobson, A. J.; Lewandowski, J. T.; Newsam, J. M. Antiferromagnetism in YBa<sub>2</sub>Cu<sub>3</sub>O<sub>6+x</sub>. *Phys. Rev. B: Condens. Matter Mater. Phys.* **1988**, *38*, 2477–2485.
- (53) Tranquada, J. M.; Cox, D. E.; Kunnmann, W.; Moudden, H.; Shirane, G.; Suenaga, M.; Zolliker, P.; Vaknin, D.; Sinha, S. K.; Alvarez, M. S.; Jacobson, A. J.; Johnston, D. C. Neutron-diffraction determination of antiferromagnetic structure of Cu ions in YBa<sub>2</sub>Cu<sub>3</sub>O<sub>6+x</sub> with x = 0.0 and 0.15. *Phys. Rev. Lett.* **1988**, *60*, 156–159.

(54) De Irujo-Labalde, X. M.; Amador, U.; Ritter, C.; Goto, M.; Patino, M. A.; Shimakawa, Y.; Garcia-Martin, S. 3D to 2D Magnetic Ordering of Fe<sup>3+</sup> Oxides Induced by Their Layered Perovskite Structure. *Inorg. Chem.* **2021**, *60*, 8027–8034.

(55) Martínez de Irujo-Labalde, X.; Goto, M.; Urones-Garrote, E.; Amador, U.; Ritter, C.; Patino, M. E. A.; Koedtrud, A.; Tan, Z.; Shimakawa, Y.; Garcia-Martin, S. Multiferroism induced by spontaneous structural ordering in antiferromagnetic iron perovskites. *Chem. Mater.* **2019**, *31*, 5993–6000.

(56) Jiang, H.; Gomez-Abal, R. I.; Rinke, P.; Scheffler, M. First-principles modeling of localized *d* states with the GW @ LDA + *U* approach. *Phys. Rev. B* **2010**, *82*, No. 045108.

(57) Imada, M.; Fujimori, A.; Tokura, Y. Metal-insulator transitions. *Rev. Mod. Phys.* **1998**, *70*, 1039–1263.

(58) Fujii, H.; Mihara, Y.; Mochiku, T.; Hata, Y.; Kadowaki, K. Order, disorder and superconductivity in FeSr<sub>2</sub>YCu<sub>2</sub>O<sub>6+δ</sub>. *Phys. C* **2004**, *415*, 85–93.

(59) Hata, Y.; Mihara, Y.; Mochiku, T.; Suzuki, J.; Kakeya, I.; Kadowaki, K.; Kita, E.; Yasuoka, H. Redistribution of Fe ion and superconductivity of FeSr<sub>2</sub>YCu<sub>2</sub>O<sub>6+y</sub> system. *Phys. C* **2004**, *417*, 17–24.

(60) Zunger, A.; Wei, S. H.; Ferreira, L. G.; Bernard, J. E. Special quasirandom structures. *Phys. Rev. Lett.* **1990**, *65*, 353–356.